

1 **Better constraining the geometry of faults in the**
2 **Charlevoix Seismic Zone**

3 **Oluwaseun Idowu Fadugba¹, Charles Langston¹, Christine A. Powell¹, and**
4 **Eunseo Choi¹**

5 ¹Center for Earthquake Research and Information, The University of Memphis, Memphis, TN 38152

6 **Key Points:**

- 7 • The first fault dips at an angle of 60° while the other two main rift faults dip at
8 44° and 43° , respectively. These fault geometries match the work by Powell and
9 Lamontagne (2017).
- 10 • The rift faults show a more complicated geometry than the simple three-faults model
11 in previous works, especially within the crater region.
- 12 • The rift fault to the northwest of the crater changes in strike and dip. The fault
13 dips about 60°SE outside the crater, but has shallower dips of about 33.4° and
14 34.8° within the crater.

Corresponding author: Oluwaseun Idowu Fadugba, ifadugba@memphis.edu

Abstract

The Charlevoix Seismic Zone (CSZ) is located along the early Paleozoic St. Lawrence rift zone in southeastern Quebec at the location of a major Devonian impact structure. The impact structure superimposed three major basement faults trending approximately N35°E. Previous work suggests two sets of geometries for the rift faults. One set has a uniform dip of 70°SE for all three faults while the other has 65°, 40°, and 40°SE, from north to south, respectively. Visual estimation of fault planes from over 1300 relocated hypocenters in the CSZ suggests more complex fault geometry. We apply a cumulative distribution of volume (CDV) of tetrahedra defined by closest neighbor events to remove unclustered hypocenters. The declustering algorithm involves comparing the CDV in the natural catalog to that of a randomized catalog within a spatial domain similar to the seismic zone. We apply a modified version of the Optimal Anisotropic Dynamic Clustering (OADC) algorithm to model realistic fault planes that best fit the clustered hypocenters. OADC method is a generalization of the k-means method using randomly-seeded planes to partition hypocenters into clusters. OADC uses the eigenvalue-eigenvector analysis of the covariance of hypocenter locations by minimizing the smallest eigenvalues of each cluster. The eigenvalues and eigenvectors of each cluster are related to the fault dimension and orientation, respectively. We extend the OADC method by incorporating high-quality source mechanisms of the earthquakes to specify seed planes rather than using randomly-seeded planes. Our fault models show a more complicated geometry than the simple three-faults model in previous studies, especially within the impact structure region, and support the along-strike variation in the fault dips suggested by recent study.

1 Introduction

The Charlevoix Seismic Zone (CSZ) is located along the early Paleozoic St. Lawrence rift zone in southeastern Quebec at the location of a major Devonian impact structure. The impact structure superimposed three major basement faults trending approximately N35°E. The three major rift faults in the CSZ are the Gouffre Northwest Fault, Saint-Laurent fault, Charlevoix Fault (Powell and Lamontagne, 2017; Fadugba et al., 2019). CSZ is the most active seismic zone in the southwestern Canada (Anglin, 1984) and has housed large earthquakes, up to M6.5 in 1925 (Bent, 1992) and M7.5 in 1663 (Ebel, 2011). The CSZ poses higher risks due to its history of generating M4+ earthquakes compared to the other seismic zones in the area and its proximity to densely populated cities (e.g.

47 Quebec City, Ottawa and Montreal). Other seismic zones in Eastern Canada are the Lower
 48 St. Lawrence (LSL), Ottawa-Bonnechere graben (OBQ), Western Quebec seismic zone
 49 (WQ) and the Saguenay graben (SG) (Fig. 1, Baird, McKinnon, and Godin (2010)).

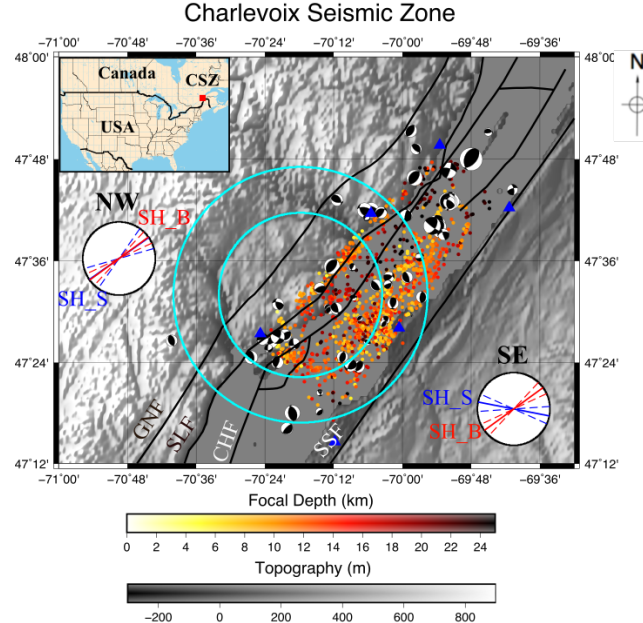


Figure 1. Topography and seismicity of the Charlevoix Seismic Zone (CSZ) showing the location of the impact structure and the seismic stations (blue triangles) (Modified after Fadugba et al., 2019). The locations of the impact structure is represented with the outer cyan circle while the more damaged inner impact structure as the inner cyan circle. Small circles are the relocated epicenters (Powell & Lamontagne, 2017) and their colors represent the focal depths. The focal mechanisms are for the earthquakes used by Mazzotti and Townend (2010) for the stress inversion of focal mechanism (SH_S) and from borehole breakout measurements (SH_B) for the earthquake clusters northwest and southeast of the crater center. Solid black lines mark the rift faults known in the region: GNF, Gouffre Northwest Fault; SLF, Saint-Laurent fault; CHF, Charlevoix Fault; and SSF, South Shore Fault (Lamontagne, 1999; Rondot, 1971). The inset shows the location of the CSZ in eastern Canada. Earthquake epicenters are from the National Resources Canada catalog for the years 1988-2011.

50 Powell and Lamontagne (2017) determined 3D V_p and V_s velocity model of the
 51 CSZ, and relocated the earthquakes using the 3D velocity model. Visual estimation of
 52 the epicenters in the CSZ shows two major earthquake clusters: the northwestern (NW)

53 and southeastern (SE) clusters. The NW clusters have earthquakes on the Gouffre Northwest
54 fault while the SE clusters comprise of the earthquakes on the Saint-Laurent and
55 Charlevoix faults (Fig. 1). Powell and Lamontagne (2017) also observed circular arcs of
56 seismicity that follow the edge of the impact structure found in 3D tomographic inves-
57 tions. The presence of damaged crustal crust from the impact crater makes the CSZ an
58 anomalous seismic zone. The presence of the impact crater should decreased the seis-
59 micity of the CSZ due to the damaged crustal rocks (Solomon et al., 1987).

60 Previous studies observed a unique distribution of earthquakes in the CSZ (e.g. Baird
61 et al., 2010) and a stress rotation in the CSZ relative to the regional first-order maxi-
62 mum horizontal stress rotation (Zoback, 2010 Mazzotti and Townend, 2010). The M4+
63 earthquakes in the CSZ are concentrated outside the crater, but on the major rift faults,
64 while the small-magnitude earthquakes are located within and beneath the crater region.
65 Despite the high level of seismicity in the CSZ, only a few earthquakes are located on
66 the southwestern part of the crater region (Fig. 1). In addition to the unique distribu-
67 tion of earthquakes in the CSZ, Mazzotti and Townend (2010) observed a significant clock-
68 wise rotation in the horizontal stress orientation derived from focal mechanisms relative
69 to the first-order regional stress orientation. Within the CSZ, stress inversion of focal
70 mechanisms of the earthquakes on the NW cluster aligns with the first-order regional
71 stress orientation while that of the southeastern cluster shows a significant clockwise ro-
72 tation relative to the NW cluster (Mazzotti and Townend, 2010).

73 Numerical modeling gives insight into the earthquake distribution and stress ro-
74 tation in the CSZ (e.g. Baird et al., 2010, Hurd and Zoback 2012, Fadugba et al., 2019).
75 However, these numerical models require a realistic but simplified fault geometry due
76 to the sensitivity of the modeled stress on the fault geometry. Previous work suggests
77 two sets of geometries for the rift faults in the CSZ. One set has a uniform dip of 70°SE
78 for all three faults (e.g. Baird et al., 2010), while the second set has 65°, 40°, and 40°SE,
79 from north to south, respectively (Powell and Lamontagne, 2017). Fadugba et al. (2019)
80 used the two fault geometries to model the stress state of the CSZ. Fadugba et al. (2019)
81 observed a partial success of modeled stress concentrations in each two fault geometries
82 in explaining the observed seismicity and stress rotations, which might suggests along-
83 strike variations in the dip angles of the rift faults. Visual estimation of fault planes from
84 over 1300 relocated hypocenters in the CSZ (Powell and Lamontagne, 2017) suggests more

85 complex fault geometry. An important research topic is whether pattern recognition al-
86 gorithm can be used to determine simplified and realistic fault geometry in the CSZ.

87 Several work has been done to determine realistic fault planes from the cloud of
88 hypocenters. For example, Ouillon et al. (2008) developed an Optimal Anisotropic Dy-
89 namic Clustering (OADC) analysis technique to delineate fault planes within the after-
90 shocks of the Parkfield earthquake sequences. The OADC method is a pattern recogni-
91 tion method aimed to reconstruct fault networks using the covariance of the spatial dis-
92 tribution of earthquakes from seismic catalogs. Ouillon and Sournette (2011) used the
93 Guassian kernel in a EM method to identify fault planes in intersecting cloud of seismic-
94 ity, hence intersecting fault planes. Wang et al. (2013b) extended the OADC method
95 to develop Anisotropic Clustering of Location Uncertainty Distributions (ACLUD). The
96 new ACLUD method incorporates some validation steps in order to give the best agree-
97 ment between the fault planes from a method similar to OADC to the observed focal mech-
98 anisms. They also used the uncertainty in the location of each earthquake in the cat-
99 alog instead of the threshold value assumed in Ouillon et al. (2008). The validation steps
100 proposed by Wang et al. (2013) produce several fault geometries that need the user's judg-
101 ment for discrimination.

102 Based on the assumption that modern seismicity in the CSZ illuminates active faults,
103 I will incorporate focal mechanisms to the Optimal Anisotropic Dynamic Clustering (OADC)
104 algorithm to determine realistic fault planes in the CSZ (Ouillon et al., 2008). I employ
105 a couple of hypotheses in this research. The first hypothesis is that modern seismicity
106 in the CSZ illuminates active faults and can be used to determine the number of the faults,
107 geometries and the interconnectivity of the fault system. The interconnectivity of these
108 faults can be used to predict the maximum magnitude earthquake in the CSZ (Harris
109 et al., 1991; Harris and Day, 1993). If modern earthquakes occur on active faults, then
110 the focal mechanisms of these earthquakes can be used to determine the style of fault-
111 ing e.g. strike-slip or reverse faulting. In other words, earthquake source mechanisms and
112 seismicity clusters define coherent fault surfaces, hence, the observed slip directions im-
113 plied by the mechanisms should also be coherent. Based on observed circular arcs of seis-
114 micity that follow the edge of the impact structure found in 3D tomographic inversions
115 (Fig. 1, Powell and Lamontagne, 2017), the second hypothesis is that the interface be-
116 tween the crater and the crust can slip and thus can cause earthquakes. High-resolution
117 focal mechanisms of moderate earthquakes (M2 – M4) will then be coupled with the Op-

118 timal Anisotropic Dynamic Clustering (OADC) analysis technique to delineate realistic
 119 fault geometries. The derived fault geometry from this study will be incorporated in
 120 future geodynamic models to determine if the modeled stress result is consistent with
 121 the regional stress field and hence provide an explanation for the seismicity of CSZ.

122 **2 Methods**

123 We use the relocated hypocenters of Powell and Lamontagne (2017) in this study.
 124 Powell and Lamontagne (2017) relocated the hypocenters, to an error of less than 1 km,
 125 using the 3-D V_p and V_s velocity models determined from a travel time tomography study.
 126 Specifically, the hypocenters were relocated with horizontal and vertical errors of 0.15
 127 km and 0.35 km, respectively. Despite the high precision in hypocenter location, the hypocen-
 128 ter shows some unclustered hypocenter probably due to the damaged crustal rocks in
 129 the impact structure (Fig. 1).

130 The method used in this study can be broadly divided into two subsections. We
 131 first perform declustering analysis on the catalog to remove isolated and diffused earth-
 132 quakes, in order to highlight the rift faults in the CSZ. Based on the diffuse nature of
 133 the background seismicity recorded in the CSZ, the seismicity in the CSZ will be sep-
 134 arated into clustered and unclustered events based on the collapsing method (Jones and
 135 Stewart, 1997) and cumulative tetrahedra volume (Ouillon and Sornette, 2011). We then
 136 apply an Optimal Anisotropic Dynamic Clustering (OADC) algorithm to model realis-
 137 tic fault planes that best fit the hypocenter data.

138 In order to avoid spurious fault plane identifications, each cluster of events will be
 139 isolated before determining optimal fault planes that minimize the thickness of the clus-
 140 ter. This is necessary because the OADC method will tend to fit the hypocenters with
 141 a near-horizontal plane when the depth extent of the earthquakes in a cluster is far less
 142 than the areal extent of the cluster.

143 The relocated hypocenters of Powell and Lamontagne (2017) have thicker cloud of
 144 seismicity about the rift faults, and some earthquakes appear to rim around the impact
 145 structure (Fig. 2C). In order to reduce the thickness of the clusters, we applied the col-
 146 lapsing method to account for the location errors in the hypocenters (Jones and Stew-
 147 art, 1997). We then applied the cumulative distribution method on the collapsed cat-
 148 alog to remove some of the hypocenters that are isolated.

149 **2.1 Declustering analyses**

150 We used two techniques to decluster the hypocenters: a collapsing method (Jones
 151 and Stewart, 1997) and the cumulative distribution of tetrahedra volume method (Ouill-
 152 lon and Sornette, 2011). The collapsing method involves moving each hypocenter within
 153 its uncertainty ellipsoid making the collapsed hypocenters within acceptable error in the
 154 earthquake location algorithm. The error ellipsoid is constructed with 99.86% confidence
 155 interval (i.e., 4 standard deviations). The idea of the cumulative distribution of tetra-
 156 hedra volume method is that the volume of a tetrahedral formed by four neighboring hypocen-
 157 ters of unclustered/isolated hypocenters will be higher than those of a clustered hypocen-
 158 ter. Given the small horizontal and vertical errors in the relocation catalog, and the dif-
 159 fuse nature of the seismicity, the cumulative distribution method has little success in sep-
 160 arating the clustered hypocenters. To solve this problem, we first applied the collaps-
 161 ing method on the catalog to reduce the variance of the earthquake distribution. and
 162 then apply the cumulative distribution method to remove any remaining isolated/unclustered
 163 hypocenters.

164 The collapsing method involves two loops: the first is on each hypocenter
 165 while the other loop is on each generation of collapsed hypocenters. We encourage the
 166 reader to see Jones and Stewart (1997) for more detailed description and limitations of
 167 the method. In summary, the collapsing method involves the following steps: (1) For each
 168 earthquake (object earthquake), we find all other earthquakes whose locations lie within
 169 the error ellipsoid of the object earthquake using $(\frac{x-x_0}{\sigma_x})^2 + (\frac{y-y_0}{\sigma_y})^2 + (\frac{z-z_0}{\sigma_z})^2 \leq s$,
 170 where s is related to the confidence interval at the specified degree of freedom. In this
 171 study, we use degree of freedom of 3, since the location of the hypocenters are in 3 di-
 172 mension. (2) Determine the centroid of the earthquakes including the object earthquake,
 173 and determine the distance and direction of the centroid to the object earthquake. We
 174 then move the object earthquake by a factor of 0.68103 of the distance and in the direc-
 175 tion to the calculated centroid (Press et al., 1986). The 0.68103 is necessary for stabil-
 176 ity (Jones and Stewart, 1997). The location of the object earthquake remains unchanged
 177 during this iteration, so the order the hypocenters are processed does not affect the re-
 178 sult.

179 The outer loop of the collapsing method involves statistical assessment of the move-
 180 ment of the hypocenters, using the following steps: (1) We store the new location of the

hypocenters as a new generation of hypocenters. (2) We normalized the movement of object earthquake by corresponding standard deviation, and (3) compare the distribution of the normalized movement with a theoretical chi distribution with degree of freedom of 3. We used chi distribution instead of chi-square distribution because the movement of the hypocenters have been normalized by standard deviation. we then repeat the collapsing method for the next generation of collapsed hypocenters while the locations and sizes of the ellipsoids of uncertainty of the original hypocenter locations remain unchanged.

We then apply a cumulative distribution of tetrahedra volume method on the collapsed hypocenters to remove unclustered hypocenters. We compare the distribution of the volumes of the tetrahedra in the collapsed (natural) catalog to the distribution of tetrahedra formed from randomized hypocenters (catalog) in a domain similar to the natural catalog. We generate the randomized catalog by randomizing the x, y and z coordinate of each hypocenter in the collapsed catalog. We randomized the hypocenter in depth as well because of the high number of hypocenters in the upper 15 km thus affecting the distribution of the tetrahedra volume in the randomized catalog. Ouillon and Sornette (2011) did not randomize the depth of the natural catalog. Following (Ouillon and Sornette, 2011), the cumulative distribution can be summarized as follows. (1) Determine the volume (V) of tetrahedra formed with quadruplets of nearest neighbor events around each hypocenter using equation (1) for both the collapsed (V) and randomized (V_0) catalogs. An apparent challenge occurs when the four nearest neighbor of an isolated hypocenter are clustered. Hence, we used three surrounding hypocenters and the object earthquake to form the tetrahedra. (2) We determine the cumulative distributions of the volumes, i.e., $N(V)$ and $N_0(V_0)$. (3) We determine the volume (V_0) of the randomized catalog corresponding to 5% quantile of the distribution, i.e., probability of 0.05. (4) We then remove all hypocenters in the natural catalog with $V > V_0$, under the assumption that the correlated hypocenters in the collapsed catalog have volumes smaller than the 5% quantile of the tetrahedra volume distribution in the randomized catalog.

$$V = \frac{1}{6} \times \begin{vmatrix} x_1 & y_1 & z_1 & 1 \\ x_2 & y_2 & z_2 & 1 \\ x_3 & y_3 & z_3 & 1 \\ x_4 & y_4 & z_4 & 1 \end{vmatrix} \quad (1)$$

209 **2.2 Modified OADC algorithm**

Ouillon et al., (2008) developed the OADC method to determine an optimal number of clusters. OADC method is a generalization of the k-means method using randomly-seeded planes to partition hypocenters into clusters. In this algorithm, we set the minimum (N_0) and maximum (N_{\max}) number of faults to use in the clustering analysis, in addition to the maximum cluster thickness (Δ) allowed in the algorithm. The value of Δ should be the same order of magnitude as the maximum radius of uncertainty ellipsoid of the hypocenters.

The algorithm starts with N_0 fault with random positions, orientations, and sizes. The value of N_0 is one in this study. In this study, we set the N_0 , N_{\max} and Δ to one, five and 0.5 km, respectively. We chose a N_{\max} value of five to account for any along-strike variation of dip angles in the crater region (Fadugba et al., 2019). We partition each hypocenter into different clusters based on its distance to the fault(s). We then determine the covariance matrix (\mathbf{C} , equation 2) of each cluster. The idea of the algorithm is to iteratively determine optimal fault planes that minimize the maximum eigenvalues of the covariance matrix. We perform a principal component analysis on the covariance matrix of each cluster to determine its eigenvectors and eigenvalues. Under the assumption that earthquakes are uniformly distributed over a fault plane, we infer the fault length, width, and thickness from the eigenvalues and the corresponding eigenvectors (Ouillon et al., 2008). This analysis is repeated until the algorithm converges to a fixed geometry. The computation stops when the maximum value of λ_3 in all the clusters is less than the value of Δ .

$$\text{Covariance matrix, } \mathbf{C} = \begin{pmatrix} \sigma_x^2 & cov(x, y) & cov(x, z) \\ cov(x, y) & \sigma_y^2 & cov(y, z) \\ cov(x, z) & cov(y, z) & \sigma_z^2 \end{pmatrix} \quad (2)$$

According to Ouillon et al., 2008, we attribute the largest eigenvalues (λ_1) to the length of the cluster, and the azimuth of the corresponding eigenvector to represent the strike of the fault. In addition, we use the intermediate (λ_2) and smallest (λ_3) eigenvalues to infer the width and thickness of the fault planes, respectively. The barycenter of each cluster (e.g., $x_b = \text{mean}(x)$) coincides with the center of the fault. Based on a statistical method, Ouillon et al., (2008) estimated the length (L) and width (W) of the fault

237 plane using $\lambda_1\sqrt{12}$ and $\lambda_2\sqrt{12}$, respectively. The value of λ_3 gives information on the
 238 thickness of the cluster. The strikes and dips of the fault planes are determined from the
 239 eigenvector of the minimum eigenvalue (λ_3) of each cluster.

240 However, if the maximum λ_3 in the stable fault geometry is greater than Δ , the
 241 fault in thickest cluster is replaced by at least two new faults with random locations and
 242 orientations within the cluster. The lengths of the new faults are one-half that of the orig-
 243 inal thick fault. We perform the splitting process several times (20 times in this study)
 244 to determine the random fault geometry that gives the least maximum λ_3 at the result-
 245 ing fixed geometry. The number of fault increases by one, and the covariance matrix anal-
 246 ysis is repeated. The simulation stops when the value of λ_3 is less than the value of Δ ,
 247 or the N_{\max} is reached.

248 In this study, we incorporate the focal mechanisms into the OADC algorithm to
 249 split the 'thick' cluster instead of using a randomly-seeded planes. We use any available
 250 high-quality focal mechanisms of earthquakes that are within or at a distance of 1 km
 251 to the thick cluster. We assign the first two dominant strike direction of the focal mech-
 252 anisms and the average of their corresponding dips to two faults. Wang et al., 2013 also
 253 incorporate focal mechanisms to OADC in their the ACLUD method, but as a valida-
 254 tion step after determining several results from OADC-type algorithm.

255 The idea is to plot the nodal plane normal vectors for earthquakes with high-quality
 256 source mechanisms and use the dominant orientations to specify the planes in the OADC
 257 method rather than using randomly-seeded planes.

258 We assigned the modal strike and penultimate strike angles to the two new faults,
 259 and use the average of all the dip angles in the focal mechanisms corresponding to the
 260 chosen strike angles.

261 3 Results

262 3.1 Declustering analyses

263 We determine the volume of the tetrahedra defined by closest hypocenters for each
 264 1329 earthquakes in the CSZ (Fig. domA, Powell and Lamontagne, 2017). The volumes
 265 of the tetrahedra ranges from 9.45×10^{-5} to about 31.61 km^3 . We also generated a ran-

domized catalog within a 65- x 65- km domain size similar to the seismic zone (Fig. domB).
 The tetrahedra volume in the randomized catalog ranges from 0.003422 to 26.74 km³.

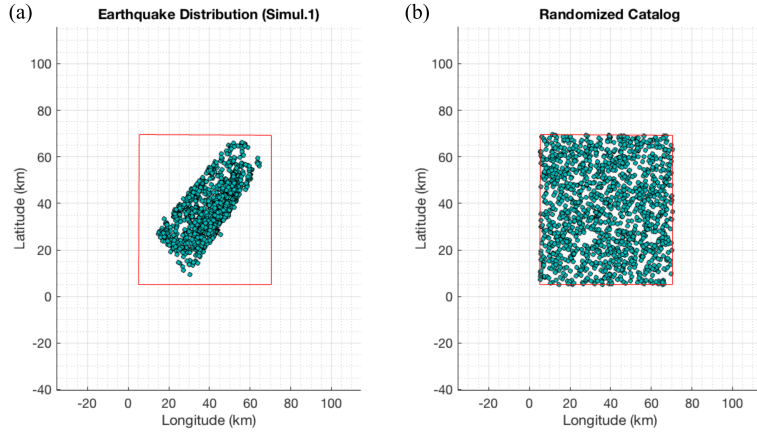


Figure 2. Domain of the seismic zone to generate randomized catalog.

We determine the cumulative distribution function (CDF) of the tetrahedra volume of both catalogs (Fig. cdf). The volume at 5 percent probability (V05) is 0.08389 km³ and the probability at target volume ($N(V05)$) = 0.5774 (Fig. cdf). This method removes 562 diffused/unclustered earthquakes (42.29% of the original catalog). Figure shows the superposition of clustered and unclustered hypocenters while figure shows only the diffuse/unclustered hypocenters. The unclustered earthquakes show no significant alignment which may depict concentration of hypocenters on main rift faults.

The clustered hypocenters occur on identifiable alignment related to the main rift faults in the CSZ (Fig. resultsb) compared to the full relocated hypocenters of Powell and Lamontagne (2017) (Fig. resultsa).

3.2 Fault plane geometry of the CSZ

Fig 6A is an intermediate result showing the best-fit plane using one fault. The plane is gently dipping to the southwest. This one fault is the thickest fault, and was splitted into two faults with one-half its original length. To generaate the two starting faults, we use focal-mechanism seeded planes rather than the randomly-seeded planes in the original OADC algorithm. We determine the strike distribution of available focal mechanisms within the thick cluster using 20 number of bins (Fig. 6B). The strike angles of the two faults are 28° and 10.8°, respectively, while their corresponding average dip angles are 55° and 62°, respectively. We generated the new fault planes, with their centers placed

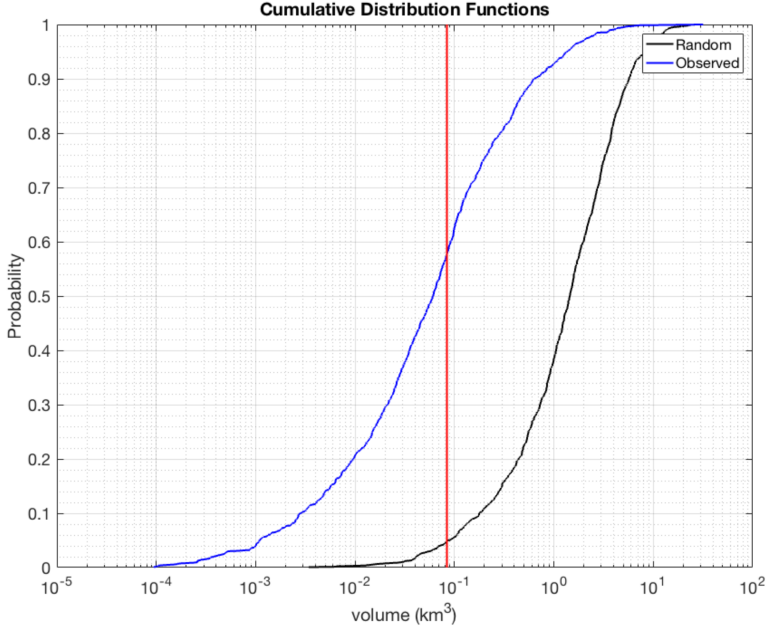


Figure 3. cumulative distribution curve for hypocenters of the earthquakes of the CSZ.

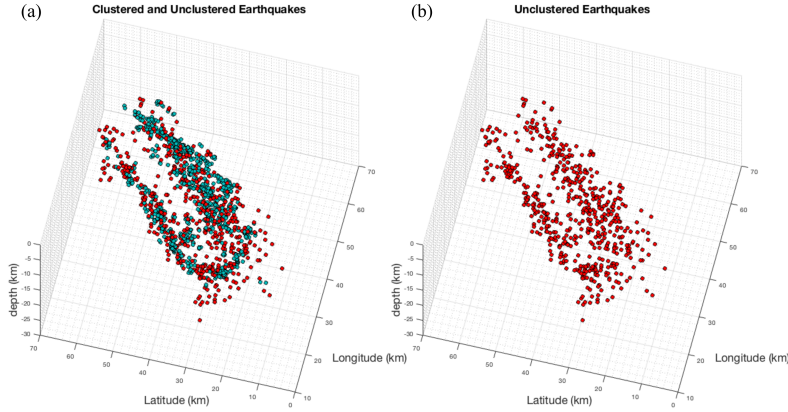


Figure 4. Unclustered hypocenters.

them at random positions within the cluster to determine the configuration with the lowest λ_3 value. We repeated the random position of the new faults 6 times in this study, to determine the positions with the best stable fault geometries assumed to be the one with the lowest λ_3 value. Figures 6 c and d show two examples of random positions of the focal-mechanism-seeded fault planes. Figure 6 e shows the intermediate stable fault plane geometries using two faults. The two faults captures the NW and SE earthquake

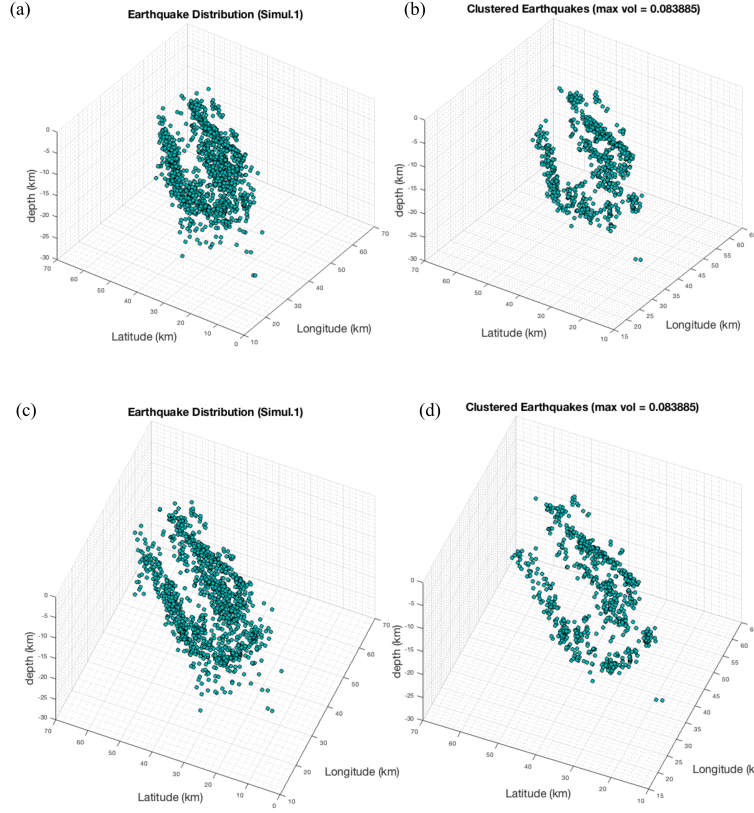


Figure 5. Clustering of earthquakes in CSZ using modified cumulative distribution method.

clusters, but with a larger minimum λ_3 values compared to the input threshold (0.001 km).

We further determine the cluster with the largest λ_3 value, and split the cluster using the above procedure. the OADC algorithm was fitted one fault to the NW and another one to the SE clusters, and also fitted the earthquakes beneath the crater with a near-horizontal fault (Fig. 7a) similar to the two-fault model in figure 6e. The near-horizontal fault in the 3-fault model was corrected when the number of fault increases to 4 (fig 7B). The intermediate fault model now distinguished the two rift faults in the SE cluster, and the NW cluster with two faults of different strike and dip angles.

got geologically feasible fault planes when the number of faults is 5 (Fig. 8). The OADC fitted the SE cluster with two fault planes with dip angles of 46.8° and 47.2° , respectively with a maximum λ_3 value of 1.5293. The NW cluster was fitted with a steeper faults with a dip of 62.9° . Within the impact structure region in the NW cluster, OADC

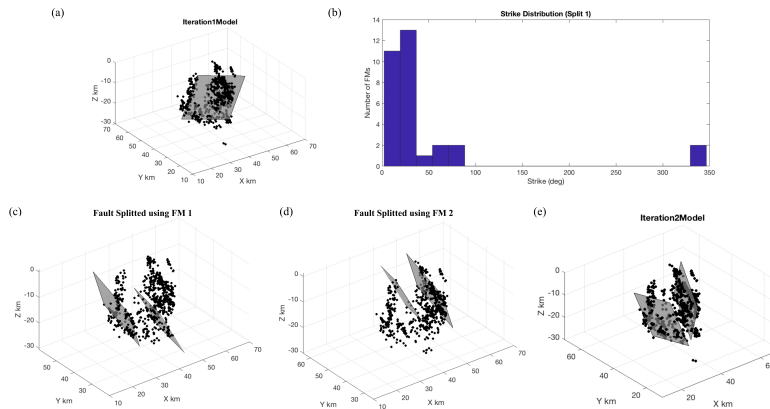
Table 1. Fault geometry of the CSZ using OADC method.

Fault No	Fault Model 1 ^a		Fault Model 2 ^a		Possible mapped fault
	Strike	Dip	Strike	Dip	
1	24.3°	48.7°	24.5°	47.3°	Charlevoix fault
2	5.8°	22.5°	8.6°	34.3°	Crater boundary
3	30.5°	57.9°	32.8°	46.8°	Saint-Laurent fault
4	24.1°	50.2°	27.8°	48.6°	Crater boundary
5	33.1°	62.9°	36.3°	58.5°	Gouffre Northwest fault

^a $\lambda_{3,max}$ for fault models 1 and 2 are 1.53 and 1.62, respectively.

303 fitted two more faults with shallower dips of 48.6° and 34.8° in the direction of the im-
 304 pact structure. Table 1 shows the summary of fault geometry from the OADC algorithm.

305 The OADC produced another geologically feasible fault geometry with a slightly
 306 higher λ_3 value of 1.6242, but with a higher dip angles for the faults in the SE cluster.
 307 The two faults dip at 46.8° and 47.2°, respectively instead of the 57.9° and 48.7° in the
 308 previous model. The NW fault also dips at an higher angle of 58.5° compared to the 62.9°
 309 in the previous model.

**Figure 6.** Intermediate fault models of OADC method on the clustered earthquakes.

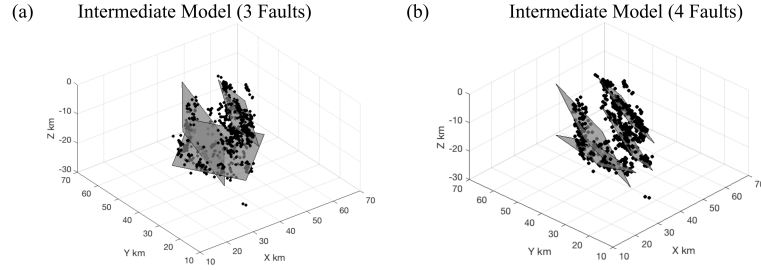


Figure 7. Intermediate fault models of OADC method on the clustered earthquakes.

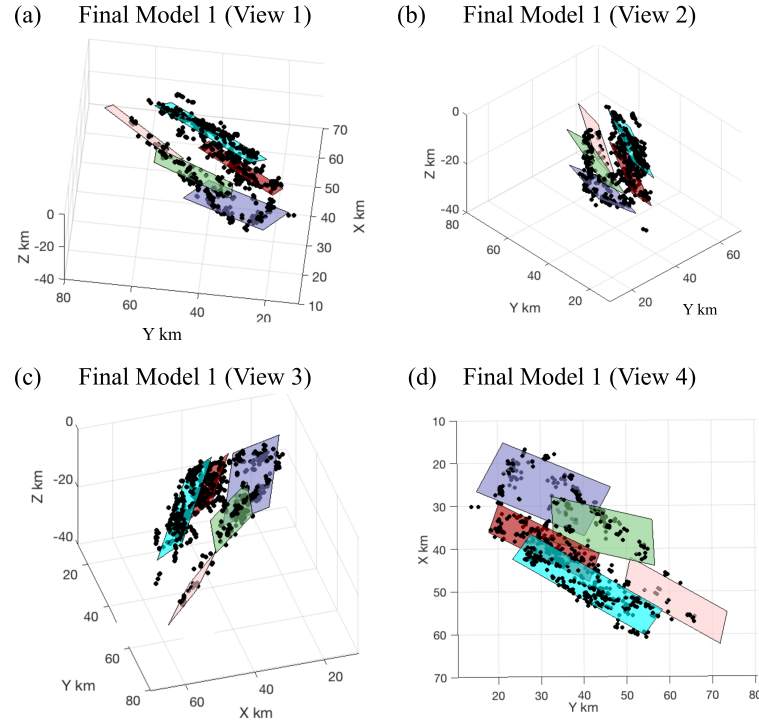


Figure 8. Final fault models of OADC method on the clustered earthquakes.

4 Discussion

In this section, we will discuss the unclustered and clustered hypocenters, and the limitations of the OADC from this study.

4.1 Unclustered seismicity

The removal of the Unclustered seismicity decrease the fuzziness of earthquake distribution in the CSZ, thereby highlighting the rift faults (Figs. 2A

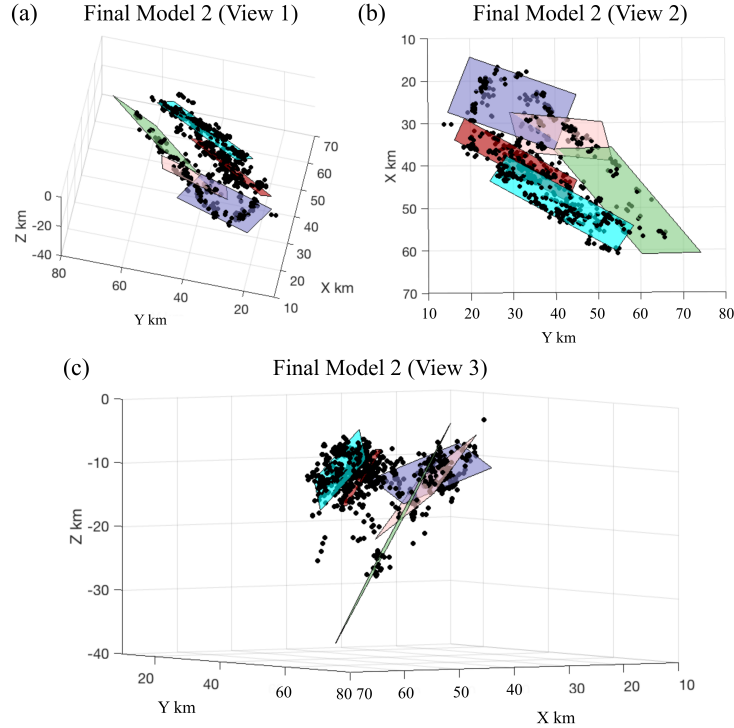


Figure 9. Final fault models of OADC method on the clustered earthquakes.

316 **and C).** The unclustered earthquakes do not have inherent structure showing the rift
 317 faults, which suggests that they do not occurred on the major rift faults in the CSZ. The
 318 lack of inherent alignment validate the declustering method has not removing clustered
 319 hypocenters. Powell and Lamontagne (2017) also shows that the rift faults can not be
 320 traced inside the crater region. In this method removes the fuzziness of the seismicity
 321 within the crater and thus, the faults can be followed all the crater within the crater re-
 322 gion. Thereby, helps to constrain the geometry of the rift faults (Fig. 2C).

323 **The unclustered seismicity in the crater region shows the geometry of**
 324 **the crater (Figs. 2B and D).** The unclustered seismicity in the crater region is the
 325 background seismicity, and is mainly within the crater region. These background seis-
 326 micity highlights the damaged region of the crater (the inner circle in Figure 1). *Cre-*
 327 *ate a 3D map of the removed seismicity to highlight the geometry of the crater.*

328 **Figure of the background seismicity showing the inner circle.**

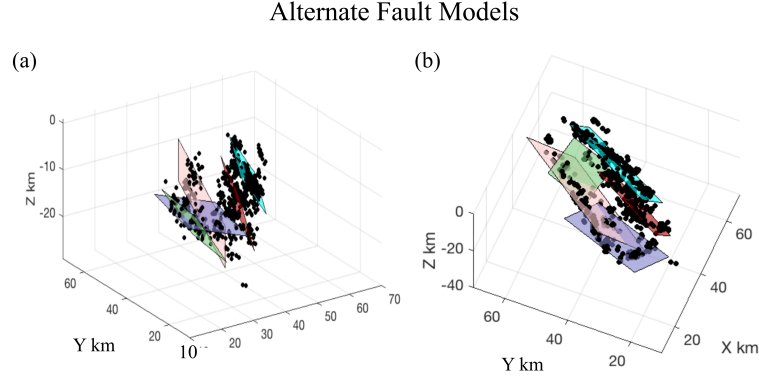


Figure 10. Alternate fault models of OADC method.

Table 2. Fault geometry of the CSZ using OADC method.

Fault No	Alternate Model 1 ^a		Alternate Model 2 ^a		Possible mapped fault
	Strike	Dip	Strike	Dip	
1	24.5°	50.2°	25.7°	47.2°	Charlevoix fault
2	177.6°	12.0°	5.8°	22.6°	Crater boundary
3	24.2°	71.4°	32.3°	50.7°	Saint-Laurent fault
4	5.7° ^b	50.3° ^b	116.3° ^c	72.47° ^c	
5	30.4°	56.3°	29.2°	50.7°	Gouffre Northwest fault

^a $\lambda_{3,max}$ for alternative models 1 and 2 are 1.59 and 1.53, respectively.

^b Possible continuation of the Gouffre Northwest fault to the southwest. ^c Spurious fault.

329

4.2 Clustered seismicity

330

The clustered seismicity show identifiable planes revealing the geometry of the three major rift faults in the CSZ (Fig. 3D). The first fault dips at an angle of 60° while the other two main rift faults dip at 44° and 43°, respectively (Fig. 4D). We need to plot the clustered earthquakes on a geologic map to see the difference. And also plot some cross-sections. The results from this study also support Powell and Lamontagne (2017) that the alignment of the earthquakes on identifiable planes suggests that the earthquakes occurred on the rift faults instead of concentrating within the fault volume as suggested by previous authors (e.g. Baird et al. 2010, Auglin, Lamontagne, Rondot). These fault geometries match the work by Powell and Lamontagne (2017). The

331

332

333

334

335

336

337

338

339 rift faults in the OADC supports that the South Shore fault do not play a role in the seis-
 340 micity of the CSZ.

341 ***In addition to the simple geometry of the rift faults, the seismicity re-***
 342 ***veals a more complicated geometry (Fig. 4D). There is a change in the strike***
 343 ***of the rift faults.*** Similar to what we see on the fault trace on Figure 1. Within the
 344 crater region, the faults are farther apart and somewhat converge in the northeastern
 345 part of the seismic zone. The middle and Charlevoix fault are closer outside the crater
 346 region. This is contrary to the simple fault geometry employed in Fadugba et al. (2010)
 347 with constant distance separation between the rift faults.

348 ***And also reveals a change of dip in the first rift faults (Fig. 3D).*** in the
 349 form of three segments. Outside the crater, the first rift fault follow the first order strikes
 350 of the rift faults. Along strike variation in the dip of the rift faults (Fadugba et al., 2019).
 351 Within the crater region, the faults dips at 33.4° and 34.8° .

352 ***The seismicity follows the crater boundary (Fig. 3D).*** especially well in the
 353 northeastern part of the crater, and the shows that the seismicity also wrap around and
 354 beneath the crater. This seismicity highlights the geometry of the crater thereby con-
 355 straining the depth of the crater.

356 Lambda3 is better to solve fitting horizontal plane fit. Show two figures showing
 357 fit with both lambda3 and global variance.

358 The shallower dip planes are in probably in response to the earthquakes wrapping
 359 around the crater region.

360 4.3 Limitation of OADC

361 ***The results of OADC algorithm may change for every run*** because the
 362 results depend on the initially random seed planes within each cluster. Therefore, we may
 363 need to repeat the algorithm several time until the fault geometry is geologically feasi-
 364 ble.

365 ***The surface projection of the fault planes from OADC may not coin-***
 366 ***cide the fault trace*** on the geologic map. We need to find out how it changes.

367 **5 Conclusions**

368 The first fault dips at an angle of 60° while the other two main rift faults dip at
 369 44° and 43°, respectively. These fault geometries match the work by Powell and Lam-
 370 ontagne (2017). The rift faults show a more complicated geometry than the simple three-
 371 faults model in previous works, especially within the crater region. Within the crater re-
 372 gion, the faults dips at 33.4° and 34.8°.

373 **Acronyms**

374 **CSZ** Charlevoix Seismic Zone

375 **SH_{max}** Maximum horizontal principal stress

376 **OADC** Optimal Anisotropic Dynamic Clustering

377 **ACLUD** Anisotropic Clustering of Location Uncertainty Distributions

378 **CDF** Cumulative Distribution Function

379 **Acknowledgments**

380 This research was supported by Center for Earthquake Research and Information, Uni-
 381 versity of Memphis.

382 **References**

- 383 Anglin, F. (1984). Seismicity and faulting in the Charlevoix zone of the St. Lawrence
 384 Valley. *Bulletin of the Seismological Society of America*, 74 (2): 595–603.
- 385 Baird, A. F., McKinnon, S. D., & Godin, L. (2010, nov). Relationship between
 386 structures stress and seismicity in the Charlevoix seismic zone revealed by 3-D
 387 geomechanical models: Implications for the seismotectonics of continental inte-
 388 riors. *Journal of Geophysical Research*, 115(B11). doi: 10.1029/2010jb007521
- 389 Bent, A. L. (1992, 10). A re-examination of the 1925 Charlevoix, Québec, earth-
 390 quake. *Bulletin of the Seismological Society of America*, 82(5), 2097-2113.
- 391 Ebel, J. E. (2011, 6). A New Analysis of the Magnitude of the February 1663 Earth-
 392 quake at Charlevoix, QuebecA New Analysis of the Magnitude of the February
 393 1663 Earthquake at Charlevoix, Quebec. *Bulletin of the Seismological Society
 394 of America*, 101(3), 1024-1038. doi: 10.1785/0120100190

- 395 Lamontagne, M. (1999). Rheological and geological constraints on the earthquake
396 distribution in the Charlevoix Seismic Zone, Quebec, Canada. *Geological Sur-*
397 *vey of Canada. Open File, D3778.*
- 398 Mazzotti, S., & Townend, J. (2010, apr). State of stress in central and eastern North
399 American seismic zones. *Lithosphere*, 2(2), 76–83. doi: 10.1130/l165.1
- 400 Powell, C. A., & Lamontagne, M. (2017, aug). Velocity models and hypocenter
401 relocations for the Charlevoix Seismic Zone. *Journal of Geophysical Research:*
402 *Solid Earth*, 122(8), 6685–6702. doi: 10.1002/2017jb014191
- 403 Rondot, J. (1971, aug). Impactite of the Charlevoix Structure Quebec,
404 Canada. *Journal of Geophysical Research*, 76(23), 5414–5423. doi:
405 10.1029/jb076i023p05414
- 406 Rondot, J. (2000). Charlevoix and sudbury as gravity-readjusted impact struc-
407 tures. *Meteoritics & Planetary Science*, 35(4), 707-712. doi: 10.1111/j.1945
408 -5100.2000.tb01454.x